D. J. Jankowski and S. W. Squyres, *Icarus* **100**, 26 (1992).
22. P. J. Mouginis-Mark *et al.*, in *Mars*, H. H. Kieffer, B. M. Jakosky, C. W. Snyder, M. S. Matthews, Eds. (Univ. of Arizona Press, Tucson, 1992), p. 424; W. B. Banerdt *et al.*, *ibid.*, p. 249; G. Schubert *et al.*, *ibid.*, p. 147.
23. M. T. Zuber and D. E. Smith, *J. Geophys. Res.*, **102**, 28,673 (1997).
24. R. J. Phillips *et al.*, *ibid.* **95**, 5089 (1990).
25. J. Phipps Morgan *et al.*, *ibid.* **100**, 8045 (1995).
26. K. L. Tanaka *et al.*, in *Mars*, H. H. Kieffer, B. M. Jakosky, C. W. Snyder, M. S. Matthews, Eds. (Univ. of Arizona Press, Tucson, 1992), p. 345.
27. S. C. Solomon and J. W. Head, *J. Geophys. Res.* **82**, 9755 (1982).
28. D. H. Scott and K. L. Tanaka, *U.S. Geol. Survey Map I-1802-A* (1986).
29. R. M. C. Lopes *et al.*, *Moon Planets* **22**, 221 (1980); P. W. Francis and G. Wadge, *J. Geophys. Res.* **88**, 8333 (1983).
30. M. H. Carr, *Water on Mars* (Oxford Univ. Press, New York, 1996).
31. G. Komatsu and V. R. Baker, *J. Geophys. Res.* **102**, 4151 (1997).
32. We use the Chezy equations [R. A. Granger, *Fluid Mechanics* (Dover, New York, 1995)] to estimate average flow velocity; v, is given by $v = C(Rs)^{1/2}$, where C is the Chezy coefficient, s is local slope, and R is hydraulic radius, defined as the ratio of flow cross-sectional area to perimeter of the wetted channel. In SI units, $C = (1/n)R^{1/6}$, where n is the Manning roughness coefficient, here square-root-gravity scaled from an assumed terrestrial value of 0.02. Hydraulic radius is obtained directly from MOLA data, assuming that the water level reached the paired-terraces and attempting to adjust the channel perimeter for post-flow mass wasting. A more difficult problem is estimation of slope. In principle, the apparent slope measured along the groundtrack can be projected into the downstream direction to yield true channel slope. The orbital track makes an angle of 50° with the downstream vector and true slope = apparent slope/cos(50°). The presence of debris flows on the channel floor could locally modify this slope.
33. This velocity and the channel depth of 1300 m yield a Froude number [$Fr = V/(hg)^{1/2}$, where h is channel depth and g is gravity] of 2.0. This value indicates supercritical flow.
34. The filter of the Viking Orbiter Camera nearest to the MOLA wavelength is red [0.5 μm to 0.7 μm; M. H. Carr *et al.*, *Icarus* **16**, 17 (1972)]. We have adopted a scaling factor of 0.8 to convert those images to 1.064 μm to be consistent with spectroscopic observations of the average martian surface in visible and infrared wavelengths [L. A. Soderblom, in *Mars*, H. H. Kieffer, B. M. Jakosky, C. W. Snyder, M. S. Matthews, Eds. (Univ. of Arizona Press, Tucson, 1992), p. 557]. It is not possible to obtain unbiased values of opacity using the above method, because the Viking images are not themselves corrected for the relevant atmospheric opacity. We used only Viking images that exhibited little or no obscuration. Such opacities in the Viking images may either darken or brighten them, unlike the effect in MOLA reflectivities, which is pure extinction. We estimated that average Viking images were darkened with an opacity of 0.4 and added this to the MOLA opacities.
35. M. C. Malin *et al.*, *Science* **279**, 1681 (1998).
36. We thank MOLA Instrument Manager R. Follas and the rest of the instrument team, and G. Cunningham, B. McAnally, and the MGS spacecraft and operation teams. We also acknowledge helpful reviews from M. Carr and an anonymous reviewer, and contributions from J. Abshire and J. Smith in instrument calibration and performance assessment, G. Neumann, G. Elman, P. Jester, and J. Schott in altimetry processing, F. Lemoine, D. Rowlands, and S. Fricke in orbit determination, and O. Aharonson, D. Brown, J. Frawley, P. Haggerty, S. Hauk, A. Ivanov, P. McGovern, C. Johnson, S. Pratt, and N. Siebert in analysis. The MOLA investigation is supported by the NASA Mars Global Surveyor Project.

15 January 1998; accepted 19 February 1998

Results from the Mars Global Surveyor Thermal Emission Spectrometer

P. R. Christensen,* D. L. Anderson, S. C. Chase, R. T. Clancy, R. N. Clark, B. J. Conrath, H. H. Kieffer, R. O. Kuzmin, M. C. Malin, J. C. Pearl, T. L. Roush, M. D. Smith

The Thermal Emission Spectrometer spectra of low albedo surface materials suggests that a four to one mixture of pyroxene to plagioclase, together with about a 35 percent dust component provides the best fit to the spectrum. Qualitative upper limits can be placed on the concentration of carbonates (<10 percent), olivine (<10 percent), clay minerals (<20 percent), and quartz (<5 percent) in the limited regions observed. Limb observations in the northern hemisphere reveal low-lying dust hazes and detached water-ice clouds at altitudes up to 55 kilometers. At an aerocentric longitude of 224° a major dust storm developed in the Noachis Terra region. The south polar cap retreat was similar to that observed by Viking.

The Thermal Emission Spectrometer (TES) investigation is designed to study the surface and atmosphere of Mars using thermal infrared (IR) spectroscopy, together with broadband thermal and solar reflectance radiometry. These observations will build upon IR observations collected by previous spacecraft, in particular the Mariner 9 Infrared Interferometer Spectrometer (IRIS) (*1*, *2*) and Viking Infrared Thermal Mapper (IRTM) investigations (*3*, *4*).

The specific objectives of the TES experiment are: (i) to determine and map the composition of surface minerals, rocks, and ices; (ii) to study the composition, particle size, and spatial and temporal distribution of atmospheric dust; (iii) to locate water-ice and CO_2 condensate clouds and determine their temperature, height, and condensate abundance; (iv) to study the growth, retreat, and total energy balance of the polar cap deposits; (v) to measure the thermophysical properties of the martian surface materials; and (vi) to characterize the thermal structure and dynamics of the atmosphere (*5*).

The TES instrument consists of three subsections: (i) a Michelson interferometer that collects spectra from 1700 to 200 cm^{-1} (~6 to 50 μm) at either 5 or 10 cm^{-1} spectral resolution, (ii) a bore-sighted bolometric thermal radiance spectrometer (4.5 to ~100 μm), and (iii) a solar reflectance spectrometer (0.3 to 2.7 μm). The TES has a noise equivalent spectral radiance near 1.2×10^{-8} W^{-1} cm^{-2} str^{-1} cm^{-1}. This corresponds to a signal-to-noise ratio (SNR) of 490 at 1000 cm^{-1} (10 μm) viewing a 270 K scene. Absolute radiometric accuracy was estimated from pre-launch data to be about 4×10^{-8} W^{-1} cm^{-2} str^{-1} cm^{-1}. However, in-flight observations indicated that a small, systematic calibration offset of $\sim 1 \times 10^{-7}$ W^{-1} cm^{-2} str^{-1} cm^{-1} is present in the TES data. This error is primarily due to slight variations in the instrument background energy between observations taken of space for calibration and those viewing the planet at an angle 90° away (*6*).

The data presented here were collected between 14 September and 30 November 1997, corresponding to orbits 2 to 53 and covering the southern spring season from aerocentric longitude (L_s) 182° to 228°. Throughout this period Mars Global Surveyer (MGS) was in a highly elliptical orbit such that the spatial resolution and observation angular velocity varied widely (*7*). During each periapsis pass the TES pointing mirror is pointed as close to nadir as possible, resulting in observations with emission angles between 0° and 30°. The spatial resolution at periapsis is as low as 1 km in

P. R. Christensen and D. L. Anderson, Arizona State University, Tempe, AZ 85287, USA.
S. C. Chase, Santa Barbara Remote Sensing, Goleta, CA 93017, USA.
R. T. Clancy, University of Colorado, Boulder, CO 80309, USA.
R. N. Clark, U.S. Geological Survey, Denver, CO 80225, USA.
B. J. Conrath, Cornell University, Ithaca, NY 14850, USA.
H. H. Kieffer, U.S. Geological Survey, Flagstaff, AZ 86001, USA.
R. O. Kuzmin, Vernadsky Institute, Moscow, Russia.
M. C. Malin, Malin Space Science Systems, San Diego, CA 92121, USA.
J. C. Pearl and M. D. Smith, Goddard Space Flight Center, Greenbelt, MD 20771, USA.
T. L. Roush, Ames Research Center, Moffet Field, CA 94035, USA.

*To whom correspondence should be addressed. E-mail: phil.christensen@asu.edu

the cross-track direction, but is 8 to 10 km down-track due to smear produced by the spacecraft velocity. Over the period observed, the local time of the periapsis observations decreased from 18.3 H (where H refers to martian hours, such that 24 H equals one martian day) to 15.7 H, while the latitude of periapsis increased from 30°N to 39°N. As a result of these viewing conditions, the near periapsis surface temperatures typically ranged from 180 to 220 K, below the 260 to 290 K temperature for which the TES was designed to observe.

During each periapsis pass the TES observes the atmosphere across the limb of the planet at several northern latitudes. These observations provide 8 km vertical resolution for a spacecraft altitude of 125 km. The TES pointing mirror is used to provide observations from the surface to a tangent point >75 km above the surface.

Away from periapsis MGS is in a 360°/100 min roll with the nadir axis pointed away from Mars. During the portion of each roll in which the TES scan plane intersects the planet, the TES pointing mirror is stepped across the planet disk, producing a raster image of Mars (Fig. 1). These observations provide views of the south polar cap at a distance of ~16,000 km, corresponding to a surface resolution at 0° emission angle of ~135 km. During the period reported, apoapsis decreased from 53,900 to 40,800 km, corresponding to an improvement in surface resolution from 460 to 350 km, the sub-spacecraft latitude varied from 30°S to 40.6°S, and the local time at the sub-spacecraft point varied from 6.4 to 3.6 H, with surface temperatures typically <200 K.

The composition of the surface minerals, dust, water-ice clouds, and atmospheric gases can be determined from the TES spectra (Fig. 2). The CO_2 band centered at 667 cm^{-1} was used to determine the atmospheric temperature-pressure profiles. Water vapor vibration-rotation bands at wavenumbers >1350 cm^{-1} and from 200 to 300 cm^{-1} were also identified. The TES spectra represent combinations of these components in varying amounts. The most prominent nongaseous spectral feature observed by the Mariner 9 IRIS was a broad absorption band between 200 and 1300 cm^{-1} produced by atmospheric dust with a maximum absorption strength near 1100 cm^{-1} (*2*). This feature was also observed by the TES (Fig. 2). Its depth increases with increasing emission angle, indicating that the feature is due to an atmospheric aerosol. Water-ice has a broad absorption below 1000 cm^{-1}, with a maximum absorption near 800 cm^{-1}, and a narrower feature with a maximum absorption near 230 cm^{-1}. The TES spectrum (Fig. 2) is similar to IRIS spectra of water-ice and matches synthetic water-ice spectra (*8*).

Four nearly consecutive spectra from Syrtis Major show a spatial pattern that indicates that the TES observed a surface deposit ~15 km in size with different spectral characteristics from the surrounding material. Previous spectral observations of Mars provided evidence for regional (50 to 300 km) variations in surface composition, in particular Phobos ISM visible/near-IR (*9*) and Viking IRTM data (*6*). However, the TES data provides evidence for compositional variability at ~10 km spatial scales.

Seven periapsis tracks have crossed over large regions composed of relatively low albedo surface materials, including three passes over Syrtis Major (Fig. 3), one over a low albedo region in Hebes Chasma (Fig. 4), and two passes over Sinus Meridiani. Spectra from these regions are similar, indicating that the surfaces are composed of similar minerals.

A spectrum of Hebes Chasma is similar to laboratory spectra (*10*, *11*) of augite, a Ca-rich clinopyroxene, in the 800 to 1350 cm^{-1} region. The identification of pyroxene is consistent with previous visible/near-IR Earth-based (*12*–*15*) and spacecraft (*9*, *16*) observations. The depths of the absorptions in the 400 to 550 cm^{-1} region do not match the laboratory spectra, although the subtle feature near 475 cm^{-1} is similar to the features seen in the augite spectrum

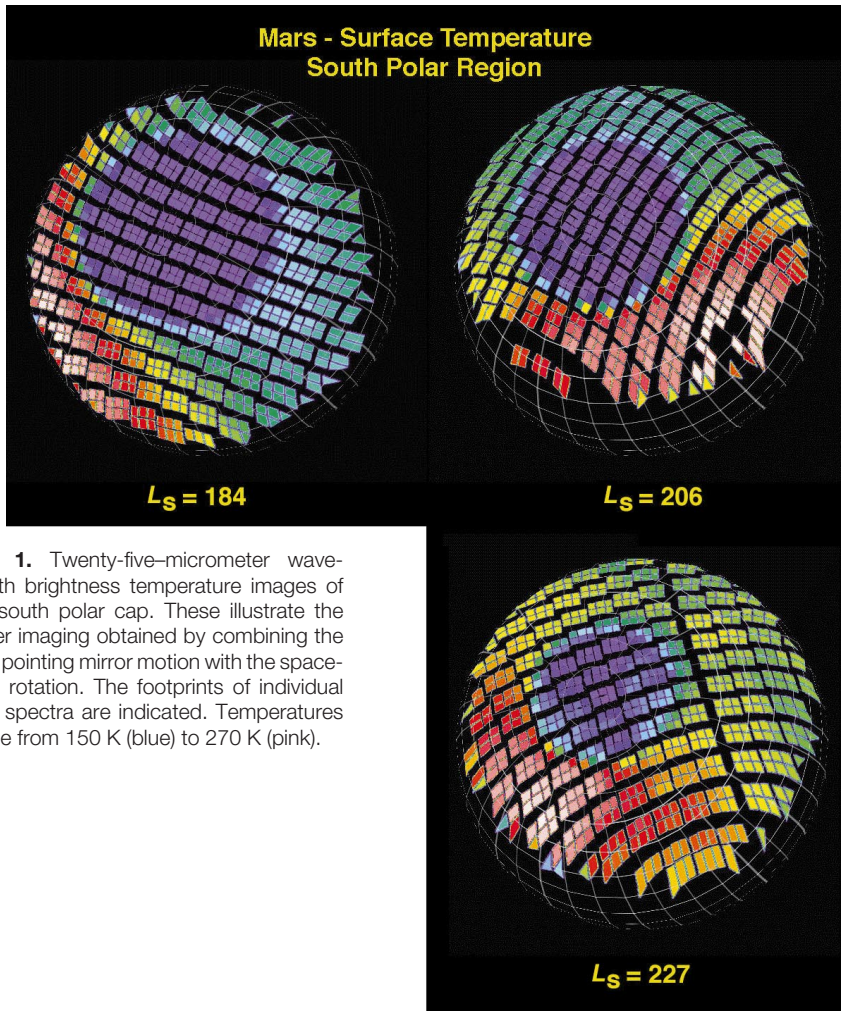

Fig. 1. Twenty-five–micrometer wavelength brightness temperature images of the south polar cap. These illustrate the raster imaging obtained by combining the TES pointing mirror motion with the spacecraft rotation. The footprints of individual TES spectra are indicated. Temperatures range from 150 K (blue) to 270 K (pink).

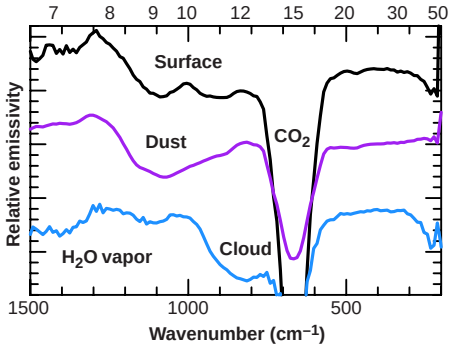

Fig. 2. General spectral classes observed by the TES. Surface, atmospheric dust, and atmospheric water-ice clouds have been observed as approximate spectral end-members. These emissivity spectra were scaled and offset for clarity. The wavelength scale in micrometers is indicated along the upper axis.

(Fig. 3). These differences in the spectral contrast between the 800 to 1350 cm^{-1} region and the 400 to 550 cm^{-1} region, as compared to laboratory data (Fig. 3), are not understood at this time. The surface reflection of downwelling atmospheric radiation, which is peaked at between 300 cm^{-1} and 450 cm^{-1} for atmospheric materials at temperatures between 160 and 240 K, may provide a partial explanation.

Other minerals, in addition to pyroxene, are required to account for all of the features observed in the TES spectra. In particular, additional materials with absorptions between 1150 and 1250 cm^{-1} and between 975 and 1050 cm^{-1} are required. Linear deconvolution (*17*) of the TES spectra gives a best-fit mixture of 45% augite, 7% bronzite (an Mg-rich orthopyroxene), 12% labradorite (a plagioclase feldspar), and 36% atmospheric dust component (Fig. 5). These abundances are interpreted to be the areal fraction of each component. Again, the absolute depth of the spectra do not match in the 400 to 550 cm^{-1} region. These results suggest that a significant amount of feldspar is present on the martian surface. The spectrum from Hebes Chasma has been used to estimate the upper limit abundances of carbonate (calcite, <10%), olivine (forsterite, <10%), clay minerals (<20%), and quartz (<5%).

A four to one mixture of pyroxene to plagioclase provides the best fit for the surface materials in Hebes Chasma. Both clino- and orthopyroxenes appear to be present, with clinopyroxene making up 85% of the total pyroxene. Dust is an important component, either on the surface or in the atmosphere. If the dust is all in the atmosphere, then the surface is composed of 80% pyroxene and 20% plagioclase. The presence of pyroxene and plagioclase is consistent with the bulk composition of most of the martian meteorites (*10*, *16*, *18*).

The low albedo materials are relatively free of weathering products, including hematite and clay minerals. These observations suggest that the low albedo materials on Mars are relatively pristine samples of igneous rocks. The estimated low abundances of calcite (<10%) in the limited regions observed indicates that carbonates are not ubiquitous on the martian surface and, if present, occur in specific locations that either favored their initial deposition or their subsequent preservation.

A map of the relative spatial variation of the pyroxene-rich component was made using a spectral shape characterization. This method determines a curvature parameter in the emissivity (ε) spectrum from 900 to 1100 cm^{-1} that is related to the depth of the pyroxene band using:

$$\text{Curvature parameter} = \frac{\left(\frac{\varepsilon 900}{\varepsilon 1000}\right)}{\left(\frac{\varepsilon 1000}{\varepsilon 1100}\right)}$$

where the subscripts refer to the wavenumber (Fig. 3). This parameter increases as pyroxene abundance increases (Fig. 6). The spatial variability in the spectral properties shows a correlation with surface morphology and albedo. In particular, the pyroxene abundance increases from bright surfaces in Isidis into Syrtis Major and decreases toward the Hellas Basin. Localized patches of low albedo material have higher abundances of the pyroxene and plagioclase mixture, indicating either a concentration of these minerals by reworking, or an absence of obscuring dust on the surface.

Atmospheric temperature profiles were obtained from 10 cm^{-1} resolution measurements within the 15-μm CO_2 absorption band using a constrained linear inversion algorithm (*19*). The necessary atmospheric slant-path CO_2 transmittances were prepared using absorption coefficient distribution functions derived from line-by-line monochromatic calculations. The required surface pressures are derived from elevations relative to the nominal 6.1 mbar surface taken from the USGS Digital Topographic Map, with an adjustment for the seasonal CO_2 sublimation cycle (*20*). For nadir-viewing spectra, profiles were obtained from the surface up to about the 0.1 mbar level with a vertical resolution of about 0.75 pressure scale height. The formal 1σ random error due to instrument noise propagation in individual spectra is ≤1 K at all levels. By combining several thousand individual retrievals from a portion of a single orbit, meridional cross sections were constructed (Fig. 7A). The observed thermal structure agrees qualitatively with Mars general circulation modeling results for similar seasonal conditions (*21*).

On a rapidly rotating planet, away from the equator, the large-scale zonal (east-west) atmospheric motion can be described by a so-called "gradient-wind" in which the

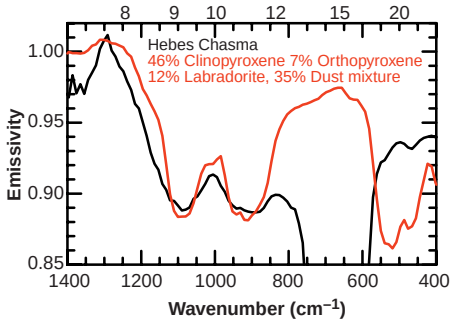

Fig. 5. Comparison of low albedo surface spectrum with a linear mixture of 45% augite, 7% bronzite, 12% labradorite, and 35% atmospheric dust. The single TES spectrum has been filtered by three samples to reduce noise.

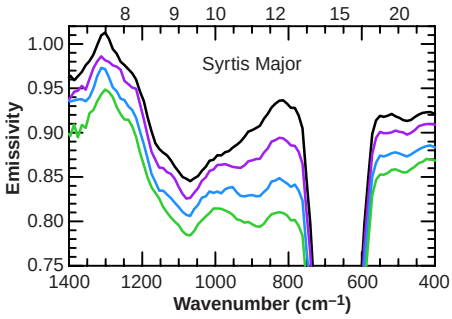

Fig. 3. Four spectra from Syrtis Major showing compositional variations present on spatial scales of ~10 km. These data were acquired with a spatial resolution of 8 km by 8 km acquired between 12°S and 13°S near 296°W during periapsis pass 34. A boxcar filter three samples wide has been applied to reduce noise and the spectra have been offset for clarity.

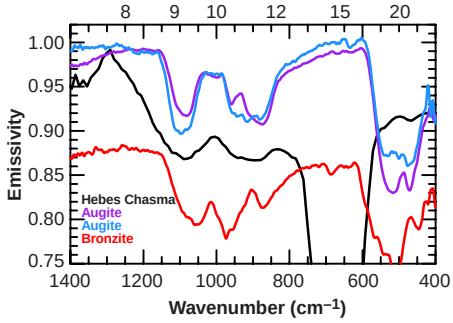

Fig. 4. Comparison of low albedo surface material within Hebes Chasma to laboratory emission spectra of two augites selected to indicate the range of spectral variability within the augite composition field and orthopyroxene bronzite. The single TES spectrum has been filtered by three samples to reduce noise. The Hebes Chasma spectrum was acquired at 0.9°S, 76.3°W on orbit 35.

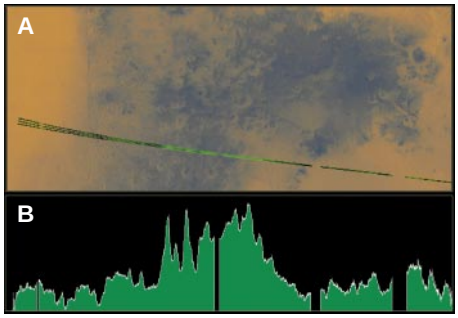

Fig. 6. Spatial variation of the pyroxene-rich component within the Syrtis Major/Terra Tyrrhena region from 28°N to 33°S between 275°W and 305°W. (**A**) The data are superimposed on the USGS digital color image of Mars. North is toward the right. (**B**) A spectral curvature index indicative of the pyroxene absorption is shown for all six TES detectors.

north-south pressure gradients are balanced by Coriolis and centrifugal forces. Assuming hydrostatic balance in the vertical direction, the zonal wind field can be calculated from the north-south temperature gradients (Fig. 7B). We assumed that the wind speed is zero at the planetary surface and, because the gradient-wind approximation is invalid near the equator, no wind speeds are shown between ±12° latitude. The strong winds centered near 55°N (Fig. 7B) represent an intense circumpolar vortex associated with the large temperature gradients at high northern latitudes in the fall hemisphere. At altitudes above the 1 mbar pressure level, temperatures increase from the equator to 45°N. This is not expected for an atmosphere in radiative equilibrium and indicates the response of the temperature field to atmospheric motions. The temperature maximum may be a result of adiabatic compression and consequent heating from the downward branch of a meridional circulation (Hadley cell) with accompanying upwelling at low southern latitudes. This heating, combined with radiative cooling of the polar regions, may maintain the temperature gradient poleward of about 50°N, which is associated with the high-speed vortex. Since orbit insertion (L_s = 180°), winds in the vortex have tripled, and the vortex moved northward ~10°.

The strength of the spectral signatures of dust are correlated with emission angle, indicating that a large proportion of the dust is suspended in the atmosphere. These signatures were used to infer column-integrated opacity as a function of location and time. Using the derived temperature profiles and surface temperature estimates obtained from the nearly transparent spectral region near 1300 cm^{-1}, optical depths of the dust were determined for several points in the spectrum. We assumed that the dust was uniformly mixed vertically in the atmosphere and that the surface emissivity is unity. The dust opacities were determined most accurately when there was a significant difference between the surface temperature and the mean atmospheric temperature in the lowest scale height of the atmosphere. Figure 8 shows a map of the average column-integrated dust opacity observed between 5 October and 21 October 1997. Most of the horizontal structure is caused by topographical features. The more dusty (dark) areas are topographic lows such as Hellas basin at 45°S latitude, 290°W longitude, and the less dusty (light) areas are topographic highs, such as the Tharsis region centered at the equator and 120°W longitude. These column-integrated opacities are consistent with the dust opacities at visible wavelengths derived from the Pathfinder camera (*22*) when the appropriate conversion from IR to visible opacity (*23*– *25*) is taken into account.

If the dust is uniformly distributed in the

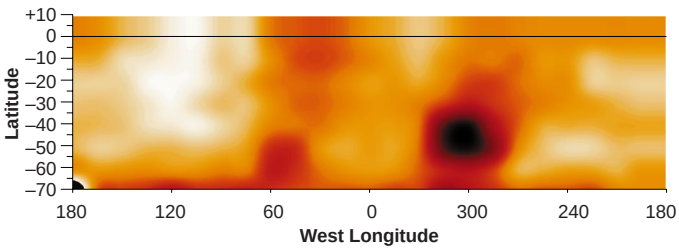

Fig. 8. The average dust opacity between 1000 to 1100 cm^{-1} for orbits 14 to 25 (5 October to 21 October 1997; L_s = 199.0° to 202.7°). Opacities range from 0.10 (white in the figure) to 0.35 (black).

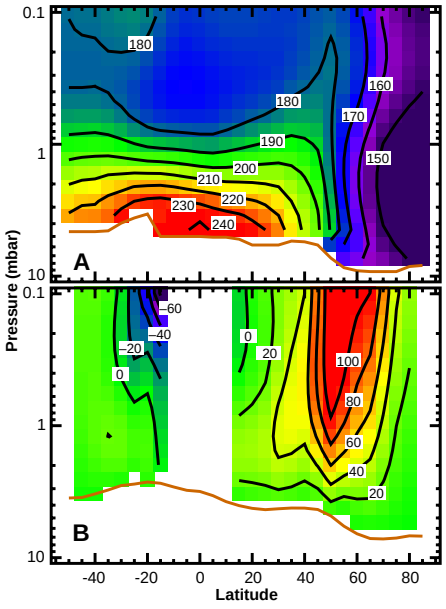

Fig. 7. (**A**) Temperatures (in kelvin) near 19 H local time from ~5000 individual retrievals of TES infrared spectra during the orbit 26 drag pass (L_s = 204°). The cross section was constructed using a sliding boxcar average 5° wide in latitude. The red line at the bottom of the temperature field represents the mean surface pressure used in the retrievals. The temperature structure is typical of this northern fall season. (**B**) The zonal (east-west) component of wind velocity computed from the retrieved temperatures shown in (A). Wind speeds are shown in meters per second, with positive values representing winds that move from west to east.

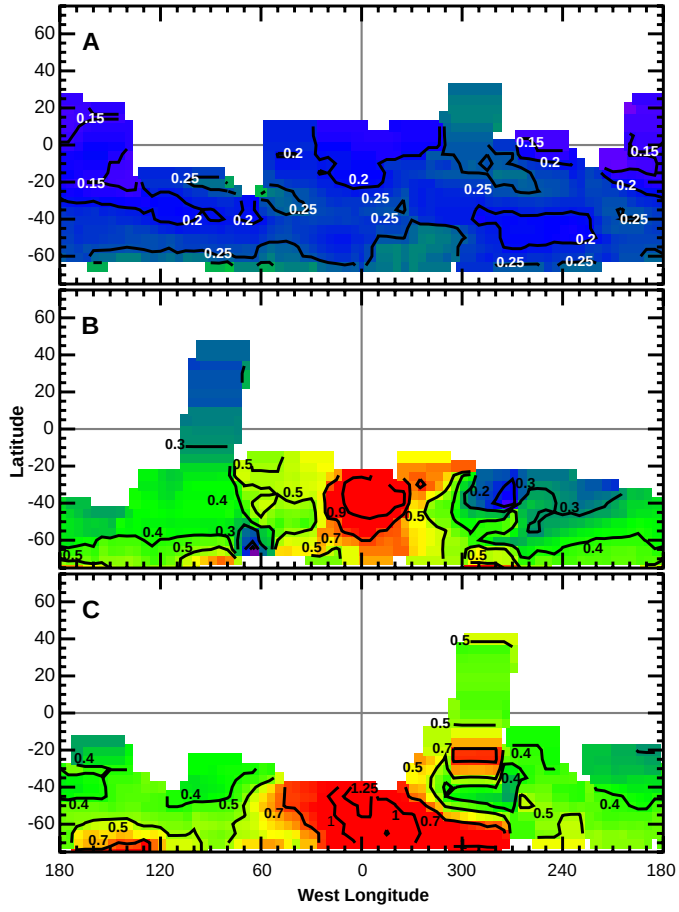

Fig. 9. Variation of the spatial distribution of atmospheric dust with time. The dust opacities are averaged over 1000 to 1100 cm^{-1} and have been scaled to an equivalent 6.1 mbar surface. Opacities range from 0.15 (violet) to 1.25 (red) (**A**) The dust opacity retrieved during orbit 25 (21 October 1997; L_s=202.7°). (**B**) The dust opacity retrieved during orbit 51 (27 November, 1997; L_s=227.3°) just after the Noachis Terra dust storm erupted. (**C**) The dust opacity retrieved during orbit 53 (30 November 1997). The dust storm has expanded and intensified and a secondary area of dustiness is observed north of the Hellas basin at about 20°S latitude and 290°W longitude.

atmosphere, the effect of topography can be removed from the dust opacity data by scaling to an equivalent 6.1 mbar surface. Examples of scaled column-integrated dust opacity maps from three selected orbits (Fig. 9) illustrate the variations in dust loading that have occurred. The dust opacity retrieved on 21 October 1997 was nearly spatially uniform, with an optical depth of 0.20 to 0.25 (Fig. 9A); transient dust activity (optical depths to 0.5) then began appearing occasionally near the receding cap edge. Beginning on orbit 49 (L_s = 224°; 25 November), the TES began observing an increase in the temperature of the lower atmosphere and an increase in atmospheric dust opacity. This activity developed over the next few days to a storm of regional extent. On 27 November, shortly after the dust storm had started in the Noachis Terra region, scaled optical depths of order unity covered an area that extended about 50° in longitude, centered near the zero meridian, and from 20°S to 60°S latitude (Fig. 9B). The dust opacity far from the storm was also elevated (typically 0.35) compared to that observed on 21 October. By 30 November, when the storm had expanded and intensified further, the core area had extended to the southeast, and a secondary area of dustiness was present north of the Hellas basin at about 20°S, 290°W (Fig. 9C). Thereafter, expansion to the southeast continued, resulting in another region of persistent activity centered near 60°S, 240°W. Other new, less active sites near 60°S, 90°W and 65°S, 160°W waxed and waned through the first 10 days of December. Subsequently, all activity equatorward of 65°S gradually ceased. By the third week of December, the background dustiness in the southern hemisphere, which had reached opacities of about 0.5 to 0.6, was declining. By 10 January 1998 (orbit 88, L_s = 235°), overall levels were at their prestorm values, with only scattered transient activity at high southerly latitudes.

Limb spectra were used to obtain temperature profiles to higher altitudes (~70 km) and with better vertical resolution (~0.5 pressure scale height) than can be obtained from nadir observations. Discrete water-ice clouds were detected and quantitatively analyzed using limb data (Fig. 10). Measurements in the CO_2 band were used to retrieve a temperature profile (Fig. 10A). Water ice displays a number of spectral features with one of the strongest centered near 230 cm^{-1}. The radiances within this absorption band at 243 cm^{-1} show distinct vertical structure (Fig. 10B); these were used along with the temperature profile to retrieve the ice number density profile (Fig. 10C). Discrete clouds centered at 45 and 53 km altitude are evident. Detached ice clouds are frequently observed in limb spectra acquired in the northern hemisphere during the fall season considered here.

The low temperatures of the martian winter poles represent a challenging target for thermal spectroscopy. At 145 K the SNR is <60 at all wavenumbers and is <1 beyond 1200 cm^{-1}. Therefore, corrections for small radiance errors are important (*26*). To mitigate the low SNR for single spectral points, TES spectra were used to synthesize a seven-band thermal emission mapper, with the bands tailored to fit this application; these include a dust band and adjacent continuum bands, "red" and "blue" surface bands where the atmosphere is relatively clear, and a split atmospheric temperature band (*27*). In addition, some of the IRTM bands (*28*) were synthesized; the corresponding brightness temperatures are labeled T_{20}, T_{11} and so on, where the subscript indicates the effective wavelength in micrometers.

Within the CO_2 cap (T_{20} < 155 K and T_7 < 205 K) and near the cap edge, where the atmosphere is warmer than the surface, particulates in the atmosphere were seen in emission (Fig. 11). The small increase in brightness temperature from 300 to 250 cm^{-1} is attributed to water-ice clouds (*8*). An average "cloud" spectrum, based on T_{11}-T_{20} > 7 K, shows strong dust and water-ice features. In contrast, an average spectrum from the warm frost-free region surrounding the cap (180 K < T_{20} < 210 K) is relatively featureless; opacities derived under such conditions have large uncertainty.

From L_s = 185° to 223°, the seasonal

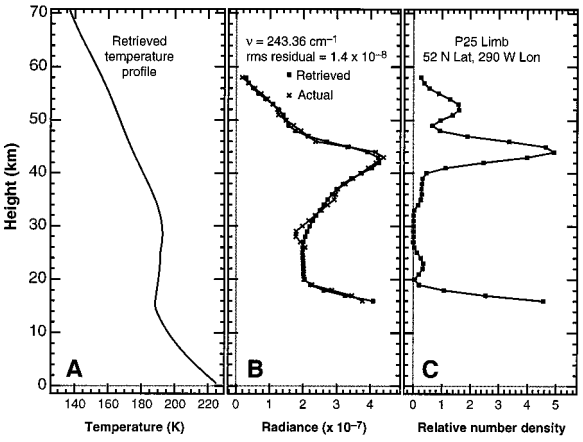

Fig. 10. Limb observations of clouds showing the vertical thermal and aerosol structure at 52°N, 290°W that was obtained by projecting the 2 × 3 detector array on the limb at successively greater altitudes above the planetary surface on orbit 25 (21 October 1997; L_s=202.7°). (**A**) The temperature profile retrieved from the TES limb observations. (**B**) The observed radiance as a function of height compared with that computed using the retrieved ice profile shown in (C). (**C**) The retrieved number density of the ice cloud as a function of height.

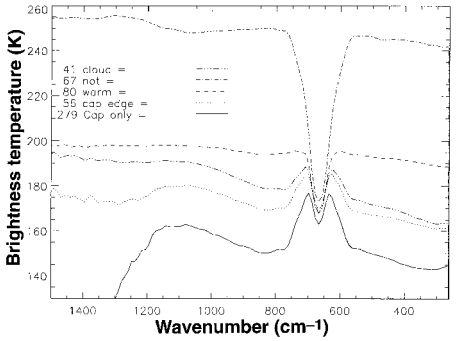

Fig. 11. Averaged TES spectra average for each of several conditions in the south polar region. Data are from one roll observation at L_s = 212°. The curve labeled "Cap only" is an average of 279 spectra where frost coverage is thought to be complete. At these temperatures, the spectral radiance for ν > 1100 cm^{-1} is not measurable by TES. For low surface temperature, the 15 μm CO_2 gas band (570 ν < 770 cm^{-1}) appears in the emission. The consistency of the brightness temperature at 670 cm^{-1} indicates that the upper atmospheric temperature drops only about 10 K over the polar cap. Atmospheric dust (850 < ν < 1350 cm^{-1}) appears in the emission, as do water-ice clouds (ν < 320 cm^{-1}). The cap edge curve is an average of 56 spectra near the edge of the cap. The warm curve is the average of 80 spectra of frost-free ground surrounding the polar cap. The cloud curve is the average of 41 spectra with strong contrast between 11 and 20 μm. The hot curve is an average of 67 spectra well off of the cap where T_{20} > 210 K.

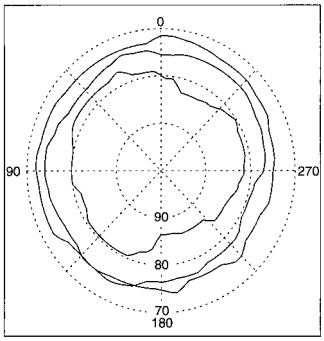

Fig. 12. Location of the south polar cap at several seasons. The edge is defined by T_{20} = 165 K in the daytime. Seasons are L_s = 192° (outer curve), 206° and 222°. Data from four consecutive orbits have been combined at each season to improve longitude coverage. The apparent reversal near 150°W is probably an artifact of irregular coverage. By L_s = 222°, the asymmetric cap extension toward 40°W is clearly established.

south polar CO_2 cap retreated continually, and the atmosphere above the cap gradually warmed. There were indications of local, temporary incursions of moderately dusty ($\tau \sim 0.25$) air over the cap, with atmospheric dust generally being greatest near the cap edge. The outer few hundred kilometers of the cap do not appear as a blackbody at the expected CO_2 condensation temperature, but, in the spectral regions with relatively low atmospheric absorption, have brightness temperatures increasing to higher wavenumber. This behavior is indicative of a mix of frost and warmer frost-free ground, consistent with the mottled visual appearance reported for the springtime cap (*29*, *30*).

Throughout much of this period, the upper atmospheric temperature (T_{15}, equivalent to the 0.6 mbar pressure level) had a consistent thermal gradient of about 0.2 K per degree latitude away from the pole. The minimum temperature, at the pole, rose gradually from 148 K at $L_s = 185°$ to 180 K at $L_s = 225°$, then rapidly to 200 K by $L_s = 225°$. By $L_s = 222°$ the dust opacity had reached 0.3 over nearly the entire cap, and atmospheric temperatures showed a strong diurnal dependence. At this time, the T_{15} minimum was located at 75°S and 6 H. The surface brightness temperature contrast was correlated with time of day and extended over the entire cap, indicating partial frost coverage.

Early telescopic observations (*30*, *31*) had indicated that the late spring recession is not symmetric about the pole, and Mariner 9 (*32*) and Viking (*29*) observations clearly showed that the retreating edge is irregular. TES observations for pairs of orbits were combined, and the edge of the cap defined on the basis of brightness temperatures observed in the daytime between 10 and 16.5 H. Near the cap edge, the TES field of view contains a range of temperatures, and the brightness temperature increases to higher wavenumber. The cap edge was defined to correspond to the location where the temperature began increasing rapidly in latitude away from the pole (Fig. 12). This cap edge temperature was 165 K in T_{20} and 187 K in T_7. The range of cap edge latitude over all longitudes for any date in this period is significant, averaging about 6°. Even at the earliest season observed ($L_s = 185°$), the cap was discernibly asymmetric, and became more asymmetric through the observation period (Fig. 13). The cap radius we determined is smaller than reported from reflectance observations (*30*) and this difference may be the result of subpixel mixing with nonlinear weighting of the different surface components (frost and bare ground) in the IR, versus linear weighting of these components in the visible.

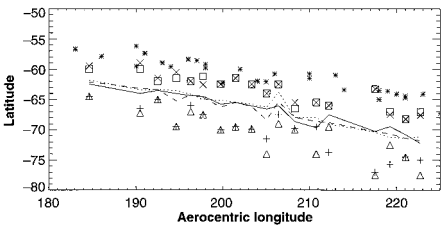

Fig. 13. Recession of the south polar cap. Symbols indicate the latitude extremes of the cap edge mapped in bands at 7 μm (x and +) and 20 μm (△ and □). The dotted line is the average of the corresponding four extremes. The solid and dashed lines represent the longitudinal average of the cap-edge latitude in the 20 and 7 μm bands. Short-term deviations, for example, near $L_s = 207°$ are due to uneven sampling of all longitudes. Prior regression data obtained at visible wavelengths are shown as asterisks; they indicate a cap of about 6° larger radius than the current thermal results.

Atmospheric particulate features were pervasive in spectra of the south polar region and cloud spectral features are strong near the edge of the retreating cap (Fig. 11). In place of the full temperature/pressure inversion used over the warmer parts of the planet, a broadband model was used. Where the surface temperatures were nearly uniform within a TES field of view, τ was estimated using an isothermal atmosphere model, where the dust was assumed to be at the atmospheric temperature near 3 mbar pressure,

$$R_d = \varepsilon_g B_{(d,T_c)} e^{-\tau} + B_{(d,T_a)}(1 - e^{-\tau})$$

where R_d is the observed radiance summed over the dust band and $B_{(d,T)}$ is the Planck function at T summed over the dust band. The surface T_c is based on the average radiance within the two continuum regions on either side of the dust band and the atmosphere temperature T_a is based on two regions in the wings of the CO_2 band. This equation is inverted to derive τ, and the vertical opacity derived using an air-mass-factor based upon the emission angle. We assumed the emissivity of all surfaces was unity.

Near the edge of the receding polar cap, a single TES field of view commonly contains materials with different temperatures and opacities derived by assuming a gray-body surface emission are misleading. We assumed the surface could be represented by a two-component system; some coverage of frozen CO_2 and a fraction of material at a higher temperature. The temperature and fraction of the other material were determined using "red" and "blue" wavelength regions (*26*) thought to be little affected by dust and where the surface emissivity is high. This two-component surface is then used to compute the upwelling radiance at the surface in the dust band.

Early in the observation period, there was little contrast between the atmospheric temperature and the surface frost, and derived opacities had a large uncertainty. At $L_s = 191.5°$ τ was about 0.15 over the cap, opacities are largest near the cap edge and over the adjacent frost-free terrain. The highest opacities are partly the result of assuming the dust is at the 3-mbar level; the associated spectra show that the highest atmospheric temperatures are closer to the surface, and, hence, the dust is probably also near the surface. By $L_s = 204°$ atmosphere/ground thermal contrast was about 15 K; localized dust clouds of opacity about 0.2 had made incursions over the cap to within 10° of the pole. At $L_s = 223.5°$ the atmosphere was about 30 K warmer than the cap and the average opacity varied from 0.1 off the cap to 0.3 over the cap. Observations with ~45 km resolution revealed dust clouds of about 200 km extent over the cap. These observations suggest that small dust storms started near the edge, and possibly within, the seasonal polar cap.

REFERENCES AND NOTES

1. R. A. Hanel *et al.*, *Science* **175**, 305 (1972).
2. B. Conrath *et al.*, *J. Geophys. Res.* **78**, 4267 (1973).
3. H. H. Kieffer *et al.*, *Science* **193**, 780 (1976).
4. H. H. Kieffer *et al.*, *J. Geophys. Res.* **82**, 4249 (1977).
5. P. R. Christensen *et al.*, *ibid.* **97**, 7719 (1992).
6. P. R. Christensen, *ibid.* **103**, 1733 (1998).
7. A. Albee, F. D. Palluconi, R. E. Arvidson, *Science*, **279**, 1671 (1998).
8. R. J. Curran, B. J. Conrath, R. A. Hanel, V. G. Kunde, J. C. Pearl, *ibid.* **182**, 381 (1973).
9. J. F. Mustard *et al.*, *J. Geophys. Res.* ***98,*** 3387 (1993).
10. V. E. Hamilton, P. R. Christensen, H. Y. J. McSween, *ibid.* **102**, 25593 (1997).
11. S. W. Ruff, P. R. Christensen, P. W. Barbera, D. L. Anderson, *ibid.*, p. 14899.
12. T. B. McCord and J. B. Adams, *ibid.* **74**, 4851 (1969).
13. R. B. Singer, *Lunar Planet. Sci.* **XI**, 1045 (1980).
14. _____ and T. L. Roush, *Bull. Am. Astron. Soc.* **17**, 737 (1985).
15. R. B. Singer and H. Y. J. McSween, in *Resources of Near-Earth Space*, J. Lewis and M. Matthews, Eds. (Univ. of Arizona Press, Tucson, AZ, 1990).
16. J. F. Mustard and J. M. Sunshine, *Science* **267**, 1623 (1995).
17. M. S. Ramsey and P. R. Christensen, *J. Geophys. Res.* **103**, 577 (1998).
18. H. Y. McSween Jr., *Meteoritics* **29**, 757 (1994).
19. R. A. Hanel, B. J. Conrath, D. E. Jennings, R. E. Samuelson, *Exploration of the Solar System by Infrared Remote Sensing* (Cambridge Univ. Press, New York, 1992).
20. J. E. Tillman, N. C. Johnson, P. Guttorp, D. B. Percival, *J. Geophys. Res.* **98**, 10963 (1993).
21. J. B. Pollack, R. M. Haberle, J. Schaeffer, H. Lee, *ibid.* **95**, 1447 (1990).
22. P. H. Smith *et al.*, *Science* **278**, 1758 (1997).
23. R. W. Zurek, *Icarus* **50**, 288 (1982).
24. T. Z. Martin, *ibid.* **66**, 2 (1986).
25. R. T. Clancy and S. W. Lee, *ibid.* **93**, 135 (1991).
26. The space background correction was computed for each observation sequence, but is still uncertain by about 5 x 10^{-8} W^{-1} cm^{-2} str^{-1} cm^{-1}. Reflected sunlight is comparable to the instrument noise level. For the south polar region, spectral radiance corresponding to that expected for solar reflectance by a Lambertian surface at the pole with albedo of 0.5 was subtracted from the TES observation before

converting to brightness temperatures.

27. Bands were formed by summing the observed radiance over a set of TES spectral points. The dust band used 30 points over 889 to 1196 cm^{-1}, the pair of dust continuum bands consisted of eight points at 772 to 846 cm^{-1} and eight points at 1238 to 1312 cm^{-1}. The surface bands were "red"; eight points at 360 to 434 cm^{-1} and blue, eight points at 1300 to 1376 cm^{-1}. The atmospheric temperature was estimated by summing two bands on each side of the 15 μm CO_2 band corresponding to a weighting function peaked near 3 mbars.
28. S. C. Chase Jr. *et al.*, *Appl. Opt.* **17**, 1243 (1978).
29. P. B. James, G. Briggs, J. Barnes, A. Spruck, *J. Geophys. Res.* **84**, 2889 (1979).
30. P. B. James, H. H. Kieffer, D. A. Paige, in *Mars*, H. H. Kieffer, B. M. Jakosky, C. W. Snyder, M. S. Matthews, Eds. (Univ. of Arizona Press, Tucson, AZ, 1994).
31. G. E. Fischbacher, L. J. Martin, W. A. Baum, *Contract 951547 Final Report, Part A, Jet Propulsion Laboratory* (1969).
32. P. B. James and K. Lumme, *Icarus* **50**, 368 (1982).

33. We wish to thank the entire TES engineering team at the Hughes Santa Barbara Research Center, led by S. Silverman and M. Greenfield, and at Arizona State University (ASU), led by G. Mehall. We thank N. Gorelick, K. Bender, S. Anwar, M. Weiss-Malik, J. Bandfield, V. Hamilton, M. Lane, S. Ruff, and K. Qazi at ASU. We thank B. Allen II, L. Fenton, A. Gordon, L. Mazzuca, W. McMillan, S. Mason Jr., K. Walker, and W. Maguire. We thank the Goddard Software Development Team, headed by S. Dason and E. Greene, including J. Guerber, K. Horrocks, M. Kaelberer, C. Martin, R. Thompson, E. Winter. We thank T. Titus and K. Mullins at the U.S. Geological Survey in Flagstaff. Finally, we thank the entire spacecraft and mission operations teams at Jet Propulsion Laboratory and Lockheed Martin.

21 January 1998; accepted 13 February 1998

The Postspinel Phase Boundary in Mg_2SiO_4 Determined by in Situ X-ray Diffraction

Tetsuo Irifune, Norimasa Nishiyama, Koji Kuroda, Toru Inoue, Maiko Isshiki, Wataru Utsumi, Ken-ichi Funakoshi, Satoru Urakawa, Takeyuki Uchida, Tomoo Katsura, Osamu Ohtaka

The phase boundary between spinel (γ phase) and $MgSiO_3$ perovskite + MgO periclase in Mg_2SiO_4 was determined by in situ x-ray measurements by a combination of the synchrotron radiation source (SPring-8) and a large multianvil high-pressure apparatus. The boundary was determined at temperatures between 1400° to 1800°C, demonstrating that the postspinel phase boundary has a negative Clapeyron slope as estimated by quench experiments and thermodynamic analyses. The boundary was located at 21.1 (±0.2) gigapascals, at 1600°C, which is ~2 gigapascals lower than earlier estimates based on other high-pressure studies.

Olivine $(Mg, Fe)_2SiO_4$, the most abundant mineral in the upper mantle, transforms to modified spinel and spinel structures at high pressure (~13.5 and ~18 GPa, at 1400° and 1500°C, respectively) and then decomposes into an assemblage of $MgSiO_3$-rich perovskite and (Mg,Fe)O ferro-periclase (at ~23 GPa and 1600°C) (*1*). The olivine–to–modified spinel and the postspinel transformations are believed to underlie the two major seismic discontinuities at 410- and 660-km depths in the mantle, respectively. Previous attempts to estimate the pressure and temperature at which the olivine–to–modified spinel transformation occurs have used quench experiments and thermodynamic analyses (*2*). Only a few experimental studies have tried to define the postspinel phase boundary (*3*, *4*), despite its importance in elucidating the nature of the 660-km discontinuity, chemical composition of the lower mantle, and dynamic processes of the subducting slabs and upwelling mantle plumes. These studies were based on quench experiments in which the pressure was estimated from calibration curves that used the phase boundaries of some reference materials (for example, covalent to metallic in ZnS, GaAs, and GaP; coesite-stishovite in SiO_2; ilmenite-perovskite in $MgSiO_3$). However, the phase boundaries of these materials have not been accurately determined, particularly at pressures above 20 GPa and at high temperatures (1000° to 2000°C) relevant to Earth's interior. Accordingly, there are uncertainties in the pressures at which a phase boundary has been observed in these quench experiments.

Several attempts were made to determine the boundaries of the phase transformations associated with the 410- and 660-km discontinuities by in situ x-ray diffraction measurements under high pressure and temperature (*5*, *6*). These studies combined a synchrotron radiation source with a multianvil apparatus, so that the temperature and pressure were simultaneously measured during the experiment with pressure scales based on the known volume changes of reference materials, such as NaCl and Au, to ensure an accurate determination of the phase boundaries. Using this technique, Morishima *et al.* determined the phase boundary between olivine and modified spinel (*5*). However, the postspinel transformations could not be determined because a single-stage multianvil system could not attain pressures higher than 20 GPa, and the run temperatures were limited to about 1500°C.

A double-stage multianvil system, with eight sintered diamond cubes used as second-stage anvils, was used to observe the ilmenite-perovskite phase boundary in $MgSiO_3$ and the postspinel phase boundary at pressures up to 28 GPa (*6*). In these studies, the uncertainty of the temperature measurement was large (±50° to 200°C), and the run temperature and the heating duration were limited to 1200° to 1300°C and 30 min, respectively, which hindered accurate determination of these phase boundaries.

A new generation synchrotron radiation facility operated at 8 GeV (SPring-8) was constructed in Hyogo prefecture, Japan, and a beamline equipped with a newly designed 1500-ton multianvil apparatus (SPEED-1500) is now available for high-pressure mineral physics studies (*7*). We developed a cell design (Fig. 1) (*8*) suitable for this system and conducted high-pressure and -temperature runs to define the postspinel phase boundary in Mg_2SiO_4 using an in situ x-ray diffraction technique.

We used pure synthetic forsterite (Mg_2SiO_4) starting material crushed and ground in a harden ceramic mortar. The powdered forsterite was mixed with a fine powder of Au (grain size ~1 μm) of 5 volume %, which was used as a pressure reference material (*9*). This mixture was pelletized and sintered in an oven at 950°C for about 12 hours and then transferred to the high-pressure furnace assembly. The whole assembly was dried at 120°C before the high-pressure and -temperature experiment so that the effect of water on the phase transformation was minimized. Pressure was applied first to up to about 28 GPa (*10*), and then the temperature was increased. During this process, x-ray diffraction data were acquired for typically 300 s by an energy-dispersive system (*11*), and the different phases were identified.

We conducted three runs at pressures between 19 to 25 GPa and temperatures be-

T. Irifune, N. Nishiyama, K. Kuroda, T. Inoue, M. Isshiki, Department of Earth Sciences, Ehime University, Matsuyama 790, Japan.
W. Utsumi, Japan Atomic Energy Research Institute, Kamigori, Ako-gun, Hyogo 678-12, Japan.
K. Funakoshi, Japan Synchrotron Radiation Research Institute, Kamigori, Ako-gun, Hyogo 678-12, Japan.
S. Urakawa, Department of Earth Sciences, Okayama University, Okayama 700, Japan.
T. Uchida, Institute for Solid State Physics, University of Tokyo, Roppongi, Tokyo 106, Japan.
T. Katsura, Institute for Study of the Earth's Interior, Okayama University, Misasa, Tottori 682-01, Japan.
O. Ohtaka, Department of Space and Earth Sciences, Osaka University, Toyonaka 560, Japan.

Results from the Mars Global Surveyor Thermal Emission Spectrometer

P. R. Christensen, D. L. Anderson, S. C. Chase, R. T. Clancy, R. N. Clark, B. J. Conrath, H. H. Kieffer, R. O. Kuzmin, M. C. Malin, J. C. Pearl, T. L. Roush and M. D. Smith

Science **279** (5357), 1692-1698.
DOI: 10.1126/science.279.5357.1692